JSTT JOURNAL OF SCIENCE AND TRANSPORT TECHNOLOGY

Journal of Science and Transport Technology
Journal homepage: https://jstt.vn/index.php/en

UNIVERSITY OF TRANSPORT TECHNOLOGY

Article info
Type of article:
Original research paper

DOI:
https://doi.org/10.58845/jstt.utt.2026.en.6.4.161-176

***Corresponding author:**
Email address:
doancv@utt.edu.vn

Received: 29/03/2026
Received in Revised Form: 01/06/2026
Accepted: 22/06/2026

Nonlinear forced vibration of higher-order shear deformable FG-GPLRC spherical shell caps with parallel stiffeners on nonlinear elastic foundation

Khuat Duc Duong[1], Cao Van Doan[2,*], Pham Duc Manh[3]
[1]School of Mechanical and Automotive Engineering, Hanoi University of Industry, Tay Tuu Ward, Hanoi, Vietnam
[2]Mechanics of Advanced Materials and Structures, University of Transport Technology, Hanoi, Vietnam
[3]Faculty of Barrack, Military Academy of Logistics, Hanoi, Vietnam

Abstract: A semi-analytical approach to investigate the nonlinear forced vibration behavior of functionally graded graphene platelet-reinforced composite (FG-GPLRC) circular plates and shallow spherical shell caps reinforced with parallel stiffeners is presented in this paper under time-dependent radial loading. The higher-order shear deformation theory is applied to establish the governing equations taking into account the von Kármán nonlinearity assumption, while a model of nonlinear visco-elastic foundation is considered to account for elastic, shear, and damping effects. The parallel stiffeners are modeled using a higher-order smeared stiffener technique. Clamped and immovable boundary conditions are assumed for both plates and shells. The total potential energy is formulated via the Lagrange approach, and the Rayleigh dissipation function is applied to model the foundation's damping. The resulting nonlinear motion equations are obtained by applying the Euler-Lagrange formulation. Time-domain responses are computed by the Runge-Kutta method, whereas frequency-amplitude characteristics are determined using the harmonic balance method. Parametric studies elucidate the significant influences of geometric parameters, material distribution, stiffener configuration, and foundation nonlinearity on the vibration behavior.

Keywords: Euler-Lagrange function, Parallel stiffeners, Nonlinear vibration, Higher-order shear deformation theory, Nonlinear elastic foundation, Rayleigh dissipation function.

1. Introduction

Circular plates are widely employed in civil structures due to their geometric simplicity and high structural efficiency, finding applications in aerospace, marine, civil, and mechanical systems. In many practical designs, circular plates are further developed into shallow spherical shell caps, whose slight curvature markedly enhances their load-carrying capacity and stiffness without significantly increasing structural weight. Owing to this advantageous balance between strength and lightweight characteristics, shallow spherical shell caps have attracted considerable attention in advanced structural applications. Consequently, understanding their mechanical behavior, particularly under complex loading and boundary conditions, remains a topic of significant scientific and practical importance.

Functionally graded materials (FGMs) have been extensively developed as advanced multifunctional composites in which material properties vary continuously through the thickness to tailor electro-thermo-mechanical performance. For axisymmetric FGM circular plates, fundamental contributions include the work of Reddy et al. [1], who employed classical plate theory, first order shear deformation theory (FSDT) and higher-order shear deformation theory (HSDT) to investigate the linear deflection response. By applying the FSDT and differential quadrature method, Ghomshei [2] further examined FGM circular plates with variable thickness considering the foundation interaction. For dynamic stress analysis, a semi-analytical formulation was proposed by Shariyat and Alipour [3] based on consistent zigzag elasticity with power series solutions for sandwich FGM circular plates. The dynamic and stability behaviors of FGM circular plates have also been widely addressed. Axisymmetric snap-through and postbuckling responses under thermal environments were analyzed [4], while vibration characteristics were studied using the generalized differential quadrature rules [5] and Chebyshev-based collocation technique in nonlinear form [6]. Strain-based finite element formulations were developed [7] for bending and linear frequency analyses of FGM square and circular plates. For shell-type structures, Shahsiah et al. [8] investigated FGM shallow spherical shell caps in the thermal buckling problem, using with simplified Sanders kinematic and Donnell-Mushtari-Vlasov theory. Deep FGM spherical shell caps were analytically examined for thermal buckling in [9] taking into account the piezoelectric actuators. By applying the Galerkin method, FGM annular spherical segments stiffened by parallel stiffeners were mentioned in linear buckling behavior [10]. In addition, sandwich and porous FGM configurations have attracted significant attention due to their enhanced load-carrying capacity [11-13].

The elastic foundation and thermal effects were considered in the sandwich FGM shallow spherical shell caps to investigate the nonlinear vibration [11, 12] based on FSDT formulations. More recently, thermo-mechanical responses of nonlinear buckling behavior of porous sandwich FGM spherical shell caps were analyzed by applying Ritz energy method and HSDT in Ref. [13], highlighting the influence of core porosity and advanced kinematic descriptions.

Functionally graded graphene platelet-reinforced composites (FG-GPLRCs) have recently emerged as a new class of high-performance nanocomposites, in which graphene platelets (GPLs) are continuously distributed through the thickness of a host matrix to achieve superior stiffness, strength, and multifunctional characteristics. Owing to the outstanding mechanical properties of graphene and the flexibility of functional gradation, FG-GPLRC structures exhibit significantly enhanced bending stiffness, stability, and dynamic performance compared with conventional composites. Extensive research has been devoted to the mechanical behavior of FG-GPLRC plates. The geometrically nonlinear deflection and stability of porous and non-porous FG-GPLRC rectangular plates were investigated by applying the differential quadrature technique [14] and finite element approach with variational differential quadrature [15]. Aeroelastic responses of FG-GPLRC plates under fluid-structure interaction were investigated by coupling finite element analysis with computational fluid dynamics [16]. For doubly curved sandwich panels, an efficient data-driven framework was proposed [17] to predict nonlinear bending under transient loading conditions. Thermal buckling, vibration, deformation, and stress analyses of FG-GPLRC annular plates were comprehensively examined using FSDT in [18], HSDT in [19], magneto-electro-elastic formulation [20], and metal foam-reinforced configurations [21, 22]. The linear and nonlinear free vibration characteristics of FG-GPLRC circular plates were studied through meshfree techniques in [23] and differential quadrature formulations in [24]. For shell-type structures, Ritz-based approaches were employed [25, 26] to investigate thermal and mechanical buckling as well as free and forced vibration of FG-GPLRC spherical shell caps, while three-dimensional analytical elasticity solutions were presented [27]. More recently, nonlinear thermo-mechanical buckling and vibration responses of stiffened FG-GPLRC spherical thin shell caps was addressed [28, 29] by refining the smeared stiffener modeling technique using the Donnell shell theory, thereby highlighting the importance of stiffener-shell interaction in advanced composite shells. The FG-GPLRC catenary shell caps were also mentioned in nonlinear thermo-mechanical buckling problems [30].

Although numerous studies have examined FGM and FG-GPLRC structures, research on nonlinear forced vibration of stiffened FG-GPLRC circular plates and shallow spherical shell caps remains limited. Existing works have mainly focused on static, buckling, or free vibration analyses, with less attention to harmonic excitation combined with geometric and material nonlinearities. Moreover, the simultaneous consideration of higher-order shear deformation, smeared stiffener modeling, and nonlinear viscoelastic foundation effects has not been comprehensively addressed. In particular, the influence of cubic foundation nonlinearity and damping on the frequency-amplitude characteristics of such structures is still insufficiently understood. Therefore, a unified semi-analytical formulation for this class of problems is still needed.

Motivated by the aforementioned research gaps, the present study aims to develop a comprehensive study for analyzing the nonlinear forced vibration of FG-GPLRC circular plates and shallow spherical shells reinforced with parallel stiffeners and with a nonlinear viscoelastic foundation. By using on HSDT combining with von Kármán nonlinearities, the formulation is established, while the stiffeners are modeled using an improved smeared stiffener technique. The governing equations are derived via the Lagrange-Euler approach, and the foundation’s damping is introduced through the Rayleigh dissipation function. The nonlinear dynamic responses are obtained using the Runge-Kutta method, and the frequency-amplitude relationships are determined by the harmonic balance method. Parametric investigations are conducted to clarify the influences of material gradation, stiffener, geometric characteristics, and foundation nonlinearity on the vibration behavior of the considered structures.

2. Modeling of FG-GPLRC circular plates and spherical shell caps

In this section, a shallow spherical shell caps with the thickness h, main radius R_0, base radius R_1 and the centripetal axis z is considered (Fig. 1). The spherical coordinate system (φ, θ, z) is simplified to the quasi-polar coordinate system (r, θ, z) with $r = R_0 \sin\varphi$, and θ and φ are the parallel and meridian coordinates. The axisymmetric displacements of spherical shell caps are considered, with the foundation's nonlinear viscoelastic interaction, and the excitation q depending on time is investigated to be harmonic and uniformly distributed on the upper surface.

For the FG-GPLRC layers, the UD, X, O, V, and Λ types of GPL distribution patterns are considered.

Five patterns of combinations for both spherical shell caps and stiffeners, as shown in Fig. 2, including

- U/U combination: U spherical shell caps, and U stiffeners

- X/X combination: X spherical shell caps, and X stiffeners

- O/O combination: O spherical shell caps, and O stiffeners

- V/Λ combination: V spherical shell caps, and Λ stiffeners

- Λ/V combination: Λ spherical shell caps, and V stiffeners

The volume fractions of GPLs in cap thickness are expressed by constant or linear functions, as $\left(-h/2 \le z \le h/2\right)$

$$W_G^{sh} = \begin{cases} W_{GPL} & \text{U type,} \\ \left[\left(4|z|\right)/h\right] W_{GPL} & \text{X type,} \\ \left[2-\left(4|z|\right)/h\right] W_{GPL} & \text{O type,} \\ \left[\left(h-2z\right)/h\right] W_{GPL} & \text{V type,} \\ \left[\left(2z+h\right)/h\right] W_{GPL} & \Lambda \text{ type,} \end{cases} \tag{1}$$

and for stiffener $\left(h/2 \le z \le h/2 + h_p\right)$

$$W_G^{st} = \begin{cases} W_{GPL} & \text{U type,} \\ \left[\left|\left(2h-4z\right)/h_p + 2\right|\right] W_{GPL} & \text{X type,} \\ \left[2-\left|\left(4z-2h\right)/h_p - 2\right|\right] W_{GPL} & \text{O type,} \\ \left[\left(h-2z\right)/h_p + 2\right] W_{GPL} & \text{V type,} \\ \left[\left(2z-h\right)/h_p\right] W_{GPL} & \Lambda \text{ type,} \end{cases} \tag{2}$$

in which W_{GPL} is the average mass fraction of GPL for both spherical shell caps and stiffeners.

The Halpin-Tsai model is used to determine the elastic moduli of the spherical shell cap and stiffeners, as [19]

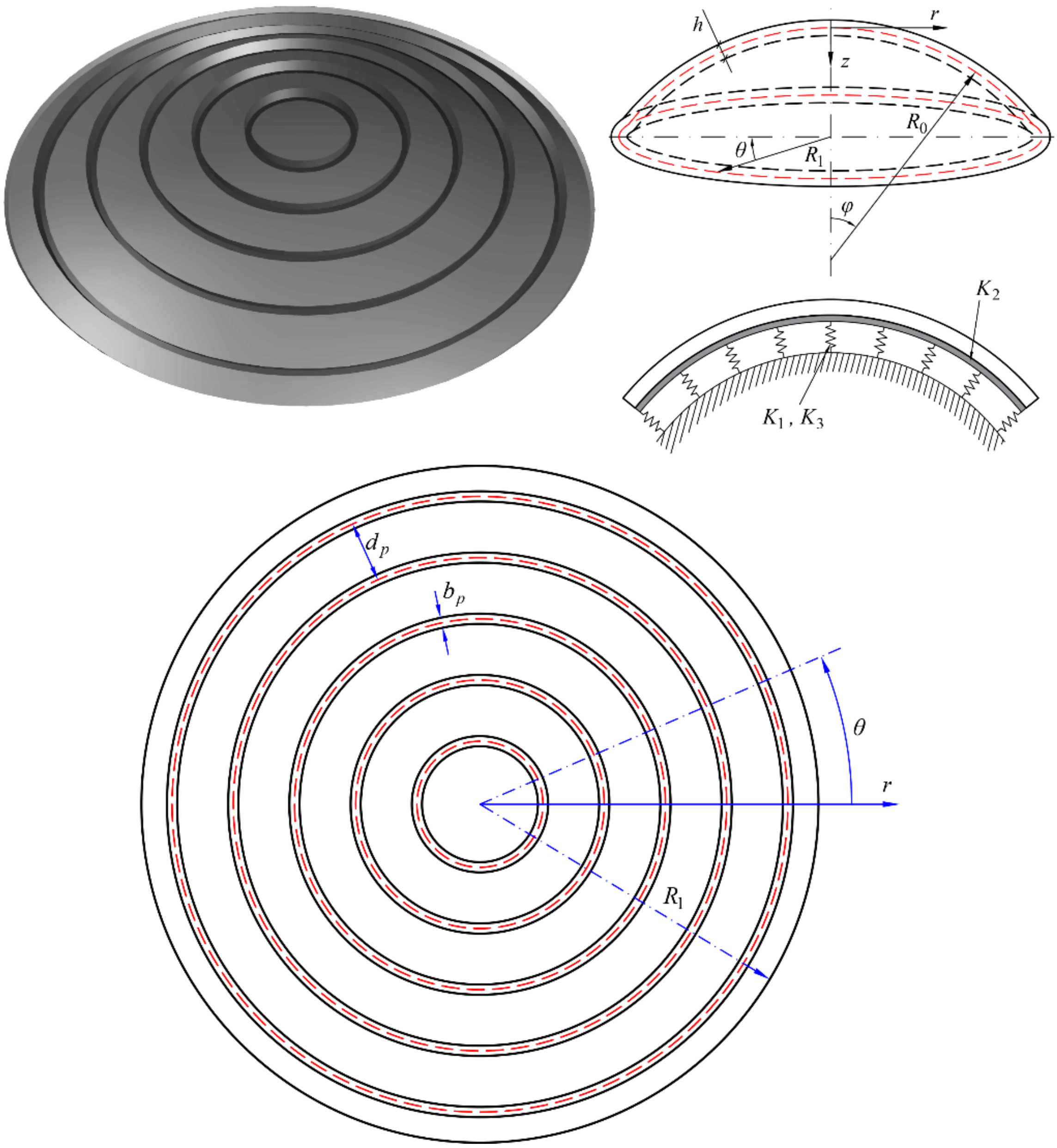

Fig. 1. Configurations and coordinate system of FG-GPLRC spherical shell caps

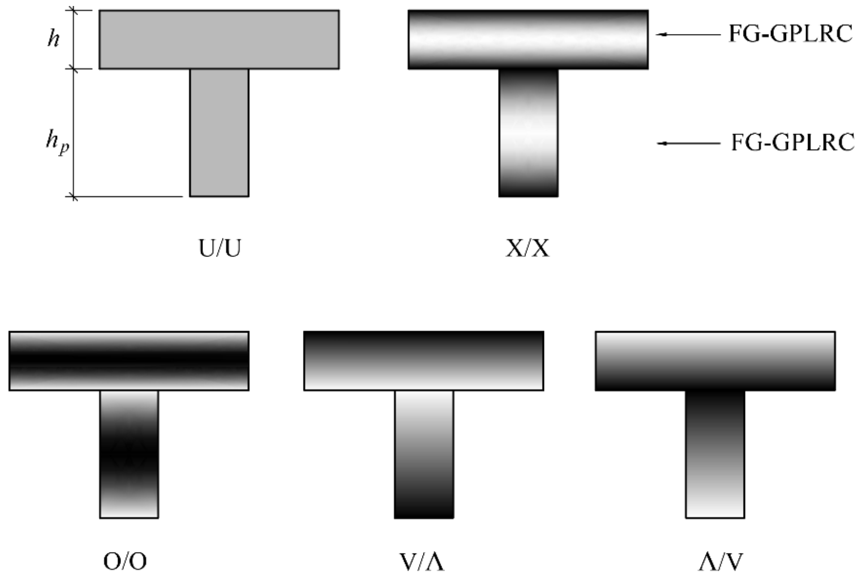

Fig. 2. Five combination patterns of material distribution of spherical shell caps and stiffeners

$$E_{sh} = \frac{E_m}{8}\left(\frac{3+3m_1n_1V_G^{sh}}{1-n_1V_G^{sh}} + \frac{5+5m_2n_2V_G^{sh}}{1-n_2V_G^{sh}}\right), \quad (3)$$

$$E_{st} = \frac{E_m}{8}\left(\frac{3+3m_1n_1V_G^{st}}{1-n_1V_G^{st}} + \frac{5+5m_2n_2V_G^{st}}{1-n_2V_G^{st}}\right), \quad (4)$$

where

$$n_1 = \frac{E_{GPL} - E_m}{E_{GPL} + m_1E_m},\ n_2 = \frac{E_{GPL} - E_m}{E_{GPL} + m_2E_m},$$

$$m_1 = 2a_G/t_G,\ m_2 = 2b_G/t_G,$$

with a_G, b_G, t_G are the length, width, and thickness of the GPLs, respectively. E_{GPL} and E_m are the Young's moduli of GPLs and the matrix, respectively, and the volume fractions of GPL in the spherical shell caps and stiffeners can be calculated as

$$V_G^{sh} = \frac{\rho_m W_G^{sh}}{\rho_m W_G^{sh} + \rho_{GPL}\left(1-W_G^{sh}\right)}, \quad (5)$$

$$V_G^{st} = \frac{\rho_m W_G^{st}}{\rho_m W_G^{st} + \rho_{GPL}\left(1-W_G^{st}\right)}, \quad (6)$$

where ρ_m and ρ_{GPL} are the densities of the matrix and the GPLs, respectively.

The Poisson's ratios, and densities of the spherical shell caps and the stiffeners are expressed according to the mixture rule as

$$\nu_{sh} = \nu_m\left(1-V_G^{sh}\right) + \nu_G V_G^{sh},$$
$$\nu_{st} = \nu_m\left(1-V_G^{st}\right) + \nu_G V_G^{st}$$

$$\rho_{sh} = \rho_m\left(1-V_G^{sh}\right) + \rho_G V_G^{sh},$$
$$\rho_{st} = \rho_m\left(1-V_G^{st}\right) + \rho_G V_G^{st}. \quad (7)$$

In this paper, the material properties of the GPLs and matrix phase, including Young's modulus, density, and Poisson's ratio, are specified based on data reported by Wang et al. [19].

Hooke's law can be employed for the FG-GPLRC structures, as follows

$$\begin{Bmatrix}\sigma_r\\ \sigma_\theta\end{Bmatrix} = \begin{bmatrix}\bar{Q}_{11} & \bar{Q}_{12}\\ \bar{Q}_{12} & \bar{Q}_{22}\end{bmatrix}\begin{bmatrix}\varepsilon_r\\ \varepsilon_\theta\end{bmatrix},\ \sigma_{rz} = \bar{Q}_{44}\varepsilon_{rz}, \quad (8)$$

where the reduced stiffnesses is determined by

$$\bar{Q}_{11}^{sh} = \bar{Q}_{22}^{sh} = \frac{E_{sh}}{1-\nu_{sh}^2},$$
$$\bar{Q}_{12}^{sh} = \frac{E_{sh}\nu_{sh}}{1-\nu_{sh}^2},\ \bar{Q}_{44}^{sh} = \frac{E_{sh}}{2+2\nu_{sh}}, \quad (9)$$

for stiffeners

$$\bar{Q}_{11}^{st} = 0,\ \bar{Q}_{22}^{st} = E_{st},\ \bar{Q}_{12}^{st} = 0,\ \bar{Q}_{44}^{st} = 0.$$

According to the HSDT, at a given distance from the mid-surface z, the axisymmetric displacements of the shells and plates are defined as [25, 26]

$$\begin{Bmatrix}\bar{u}\\ \bar{v}\\ \bar{w}\end{Bmatrix} = \begin{Bmatrix} u(r) + \phi(r)z - \dfrac{4z^3}{3h^2}\left[w(r)_{,r} + \phi(r)\right]\\ 0\\ w(r) + w^*(r)\end{Bmatrix}, \quad (10)$$

where $\phi(r)$ is the rotation, the imperfect deflection is denoted by $w^*(r)$.

The strain components are expressed at a distance z from the mid-surface, presented as Eq. (11). Applying the von Karman nonlinearity, the mid-surface strains $\varepsilon_r^{(0)}, \varepsilon_\theta^{(0)}, \varepsilon_{rz}^{(0)}$, defined as Eq. (12).

The formulations are first established for spherical shell caps, while the formulations are recovered as a limiting case by letting the principal radius tend to infinity $(R_0 \to \infty)$ for circular plates. The axisymmetric extensional forces, transverse shear forces, bending moments, higher-order components are then obtained by integrating the constitutive equations derived from Hooke's law as Eq. (13)

$$\begin{Bmatrix} \varepsilon_r \\ \varepsilon_\theta \\ \varepsilon_{rz} \end{Bmatrix} = \begin{Bmatrix} \varepsilon_r^{(0)} \\ \varepsilon_\theta^{(0)} \\ \varepsilon_{rz}^{(0)} \end{Bmatrix} + z \begin{Bmatrix} \phi_{,r} \\ \dfrac{\phi}{r} \\ 0 \end{Bmatrix} - z^2 \begin{Bmatrix} 0 \\ 0 \\ \dfrac{4}{3h^2}\left(\phi + w_{,r}\right) \end{Bmatrix} - z^3 \begin{Bmatrix} \dfrac{4}{3h^2}\left(\phi_{,r} + w_{,rr}\right) \\ \dfrac{4}{3h^2}\left(\dfrac{\phi}{r} + \dfrac{1}{r} w_{,r}\right) \\ 0 \end{Bmatrix}. \tag{11}$$

$$\begin{Bmatrix} \varepsilon_r^{(0)} \\ \varepsilon_\theta^{(0)} \\ \varepsilon_{rz}^{(0)} \end{Bmatrix} = \begin{Bmatrix} \dfrac{1}{2} w_{,r}^2 - \dfrac{w}{R_0} + u_{,r} + w_{,r} w_{,r}^* \\ -\dfrac{w}{R_0} + \dfrac{u}{r} \\ w_{,r} + \phi \end{Bmatrix}. \tag{12}$$

$$\begin{Bmatrix} N_r \\ N_\theta \\ M_r \\ M_\theta \\ P_r \\ P_\theta \end{Bmatrix} = \begin{Bmatrix} \bar{B}_{11} & \bar{B}_{12} & \bar{C}_{11} & \bar{C}_{12} & \bar{D}_{11} & \bar{D}_{12} \\ \bar{B}_{12} & \bar{B}_{22} & \bar{C}_{12} & \bar{C}_{22} & \bar{D}_{12} & \bar{D}_{22} \\ \bar{C}_{11} & \bar{C}_{12} & \bar{F}_{11} & \bar{F}_{12} & \bar{G}_{11} & \bar{G}_{12} \\ \bar{C}_{12} & \bar{C}_{22} & \bar{F}_{12} & \bar{F}_{22} & \bar{G}_{12} & \bar{G}_{22} \\ \bar{D}_{11} & \bar{D}_{12} & \bar{G}_{11} & \bar{G}_{12} & \bar{H}_{11} & \bar{H}_{12} \\ \bar{D}_{12} & \bar{D}_{22} & \bar{G}_{12} & \bar{G}_{22} & \bar{H}_{12} & \bar{H}_{22} \end{Bmatrix} \times \begin{Bmatrix} \varepsilon_r^{(0)} \\ \varepsilon_\theta^{(0)} \\ \phi_{,r} \\ \dfrac{\phi}{r} \\ -\dfrac{4}{3h^2}\left(\phi_{,r} + w_{,rr}\right) \\ -\dfrac{4}{3h^2}\left(\dfrac{\phi}{r} + \dfrac{1}{r} w_{,r}\right) \end{Bmatrix}, \tag{13}$$

$$\begin{Bmatrix} Q_r \\ R_r \end{Bmatrix} = \begin{Bmatrix} \bar{I}_{44} & \bar{I}_{45} \\ \bar{I}_{45} & \bar{I}_{55} \end{Bmatrix} \begin{Bmatrix} \varepsilon_{rz}^{(0)} \\ -\dfrac{4}{3h^2}\left(\phi + w_{,r}\right) \end{Bmatrix},$$

where

$$\left(\bar{B}_{11}, \bar{C}_{11}, \bar{F}_{11}, \bar{D}_{11}, \bar{G}_{11}, \bar{H}_{11}\right) = \int_{-h/2}^{h/2} \bar{Q}_{11}^{sh}\left(1, z, z^2, z^3, z^4, z^6\right) dz,$$

$$\left(\bar{B}_{12}, \bar{C}_{12}, \bar{F}_{12}, \bar{D}_{12}, \bar{G}_{12}, \bar{H}_{12}\right) = \int_{-h/2}^{h/2} \bar{Q}_{12}^{sh}\left(1, z, z^2, z^3, z^4, z^6\right) dz,$$

$$\left(\bar{B}_{22}, \bar{C}_{22}, \bar{F}_{22}, \bar{D}_{22}, \bar{G}_{22}, \bar{H}_{22}\right) = \int_{-h/2}^{h/2} \bar{Q}_{22}^{sh}\left(1, z, z^2, z^3, z^4, z^6\right) dz + \frac{b_p}{d_p} \int_{h/2}^{h/2+h_p} \bar{Q}_{22}^{st}\left(1, z, z^2, z^3, z^4, z^6\right) dz,$$

$$\left(\bar{I}_{44}, \bar{I}_{45}, \bar{I}_{55}\right) = \int_{-h/2}^{h/2} \bar{Q}_{44}^{sh}\left(1, z^2, z^4\right) dz.$$

By accounting for the effects of the nonlinear elastic foundation and neglecting the relatively small in-plane and rotary inertia terms, the strain energy and the work performed by external forces are respectively expressed as

$$\bar{U}_{int} = \pi \int_{-h/2}^{h/2} \int_0^{R_1} (\sigma_r \varepsilon_r + \sigma_\theta \varepsilon_\theta + \sigma_{rz}\varepsilon_{rz}) rdrdz, \tag{14}$$

$$\begin{aligned} \bar{U}_{ext} &= 2\pi \int_0^{R_1} qwrdr \\ &-\pi \int_0^{R_1} \left\{ \left[K_1 w - K_2 \left(w_{,rr} + \frac{1}{r} w_{,r} \right) + \frac{K_3 w^3}{2} \right] w \right\} rdr, \end{aligned} \tag{15}$$

$$\bar{U}_T = \pi \int_{-h/2}^{h/2} \int_0^{R_1} \rho(z) \bar{w}_{,t}^2 rdrdz, \tag{16}$$

where K_1 (N/m^3) represents the linear Winkler foundation stiffness, K_2 (N/m) denotes the linear Pasternak shear stiffness, and K_3 (N/m^5) corresponds to the nonlinear foundation stiffness. Depending on its sign, the nonlinear stiffness K_3 characterizes either a softening or a hardening foundation response.

Consequently, by combining Eqs. (14)-(16), the total potential energy of the system can be expressed as

$$\bar{U} = \bar{U}_{ext} - \bar{U}_{int} + \bar{U}_T. \tag{17}$$

3. Assumed displacement form and solution methodology

The shells are investigated to satisfy clamped and immovable boundary condition, with axisymmetric deformation condition, which can be expressed as

$$\begin{aligned} &\text{At } r = 0: \quad w = \text{finite}, \ \phi = 0, \ u = 0, \ w_{,r} = 0, \\ &\text{At } r = R_1: \ w = 0, \ w_{,r} = 0, \ \phi = 0, \ u = 0. \end{aligned} \tag{18}$$

The axisymmetric deformation assumption is justified by the combination of uniformly distributed loading, the use of circumferential stiffeners, which significantly enhance the hoop stiffness and suppress angular variation, and the shallow shell geometry, which tends to exhibit plate-like behavior. Under these conditions, the dynamic response is expected to be dominated by the axisymmetric mode. To satisfy the specified boundary conditions, the axisymmetric solution forms are employed [25, 26].

$$\begin{aligned} &u = Ur\frac{(-r+R_1)}{R_1^2}, \quad \phi = \Phi r \frac{(-r^2+R_1^2)}{R_1^3}, \\ &w = W\frac{(-r^2+R_1^2)^2}{R_1^4}, \ w^* = \kappa h \frac{(-r^2+R_1^2)^2}{R_1^4}, \end{aligned} \tag{19}$$

where the imperfection w^* is in similar form of deflection; the imperfection size is denoted by κ.

The Euler-Lagrange formulation is incorporated with the Rayleigh dissipation function, taking into account the foundation's viscous damping, as

$$\begin{aligned} &-\frac{\partial \bar{U}}{\partial W} + \frac{d}{dt}\left(\frac{\partial \bar{U}}{\partial \dot{W}}\right) + \frac{\partial d_1}{\partial \dot{W}} = 0, \\ &-\frac{\partial \bar{U}}{\partial U} + \frac{d}{dt}\left(\frac{\partial \bar{U}}{\partial \dot{U}}\right) = 0, \\ &-\frac{\partial \bar{U}}{\partial \Phi} + \frac{d}{dt}\left(\frac{\partial \bar{U}}{\partial \dot{\Phi}}\right) = 0, \end{aligned} \tag{20}$$

where the damping potential energy $d_1 = \pi \int_0^{R_1} c\dot{w}^2 rdr$, the in-plane and rotary inertia terms are neglected, as their contributions are generally small compared to the transverse inertia for the vibration characteristics considered in this study.

The equations of motion of the structures are derived by substituting Eq. (19) into the total potential energy expression in Eq. (17) and subsequently into Eq. (20), presented as

$$\bar{b}_{11}U + \bar{b}_{12}\Phi + \bar{b}_{13}W + \bar{b}_{14}W(W + 2\kappa h) = 0, \tag{21}$$

$$\bar{b}_{12}U + \bar{b}_{22}\Phi + \bar{b}_{23}W + \bar{b}_{24}W(W + 2\kappa h) = 0, \tag{22}$$

$$\begin{aligned} &\bar{b}_{31}U + \bar{b}_{32}\Phi + \bar{b}_{33}U(W + \kappa h) \\ &+\bar{b}_{34}\Phi(W + \kappa h) + \bar{b}_{35}W(W + 4\kappa h/3) \\ &+\bar{b}_{36}W(W + \kappa h)(W + 2\kappa h) \\ &+\bar{b}_{37}W^3K_3 + \bar{b}_{38}W + \bar{b}_{311}q \\ &-\frac{\pi}{5}R_1^2\left(c\dot{W} + \bar{b}_{312}\ddot{W}\right) = 0, \end{aligned} \tag{23}$$

where

$$\bar{b}_{11} = -\frac{\pi}{6}\left(\bar{B}_{22} + 2\bar{B}_{11}\right),$$

$$\bar{b}_{12} = \frac{\pi}{60}\left[\frac{4}{3h^2}\left(14\bar{D}_{22} + 34\bar{D}_{11}\right) - 14\bar{C}_{22} - 34\bar{C}_{11}\right],$$

$$\bar{b}_{13}=-\frac{4}{3h^2}\frac{\pi}{15R_1}\left(34\bar{D}_{11}+14\bar{D}_{22}\right)+\frac{\pi R_1}{R_0}\left(3\bar{B}_{11}+19\bar{B}_{22}+22\bar{B}_{12}\right),$$

$$\bar{b}_{14}=\frac{\pi}{315R_1}\left(46\bar{B}_{11}-82\bar{B}_{12}\right),$$

$$\bar{b}_{22}=\frac{\pi}{12}\left[\begin{array}{l}\frac{4}{3h^2}\left(24\bar{G}_{11}+6I_{45}R_1^2+8\bar{G}_{22}\right)\\ -\left(\frac{4}{3h^2}\right)^2\left(12\bar{H}_{11}+9R_1^2\bar{I}_{55}+4\bar{H}_{22}\right)\\ +\bar{I}_{44}R_1^2+4\bar{F}_{22}+12\bar{F}_{11}\end{array}\right],$$

$$\bar{b}_{23}=-\frac{\left[\pi\left(-3\bar{I}_{55}R_1^2-\frac{4\bar{H}_{22}}{3}-4\bar{H}_{11}\right)\left(\frac{4}{3h^2}\right)^2\right]}{R_1}-\frac{\pi\left[-\frac{R_1^2\bar{I}_{44}}{3}+\left(4\bar{G}_{11}+2\bar{I}_{45}R_1^2+\frac{4\bar{G}_{22}}{3}\right)\frac{4}{3h^2}\right]}{R_1}-\frac{\pi R_1\left[\left(2\bar{D}_{22}+2\bar{D}_{11}/3+8\bar{D}_{12}/3\right)\frac{4}{3h^2}\right]}{8R_0}-\frac{\pi R_1\left[-2\bar{C}_{22}-2\bar{C}_{11}/3-8\bar{C}_{12}/3\right]}{8R_0},$$

$$\bar{b}_{24}=-\pi\left[\left(2\bar{D}_{11}/3-2\bar{D}_{12}\right)\frac{4}{3h^2}+2\bar{C}_{12}-2\bar{C}_{11}/3\right]\Big/5R_1,$$

$$\bar{b}_{31}=\frac{\pi R_1\left(19\bar{B}_{22}+22\bar{B}_{12}+3\bar{B}_{11}\right)}{105R_0}-\frac{\frac{4\pi}{3h^2}\left(14\bar{D}_{22}+34\bar{D}_{11}\right)}{15R_1},$$

$$\bar{b}_{32}=-\frac{\pi\left(-3R_1^2\bar{I}_{55}-\frac{4\bar{H}_{22}}{3}-4\bar{H}_{11}\right)\left(\frac{4}{3h^2}\right)^2}{R_1}+\frac{\pi\bar{I}_{44}R_1^2/3}{R}-\frac{\pi\left(2\bar{I}_{45}R_1^2+\frac{4\bar{G}_{22}}{3}+4\bar{G}_{11}\right)\frac{4}{3h^2}}{R_1}-\frac{\pi R_1\left[\frac{4}{3h^2}\left(2\bar{D}_{22}+2\bar{D}_{11}/3+8\bar{D}_{12}/3\right)\right]}{8R_0}-\frac{\pi R_1\left(-2\bar{C}_{22}-2\bar{C}_{11}/3-8\bar{C}_{12}/3\right)}{8R_0},$$

$$\bar{b}_{33}=\frac{2\pi\left(-82\bar{B}_{12}+46\bar{B}_{11}\right)}{315R_1},$$

$$\bar{b}_{34}=\frac{2\pi\left[\left(-2\bar{D}_{11}+6\bar{D}_{12}\right)\frac{4}{3h^2}+2\bar{C}_{11}-6\bar{C}_{12}\right]}{15R_1},$$

$$\bar{b}_{35}=\frac{4}{3h^2}\frac{4\pi\left(2\bar{D}_{11}-6\bar{D}_{12}\right)}{5R_1^2}+\frac{4\pi\left(\bar{B}_{11}+\bar{B}_{12}\right)}{5R_0},$$

$$\bar{b}_{36}=-\pi\frac{128\bar{B}_{11}}{105R_1^2},\ \bar{b}_{37}=-\frac{R_1^2\pi}{9},$$

$$\bar{b}_{38}=\frac{\pi\left[-\frac{R_1^4K_1}{20}-4\left(\frac{4}{3h^2}\right)^2\left(\bar{H}_{11}+\frac{\bar{H}_{22}}{3}\right)\right]}{4R_1^2}+\frac{4}{3h^2}\frac{2\pi\left(\bar{D}_{11}+3\bar{D}_{22}+4\bar{D}_{12}\right)}{3R_0}+\frac{\pi R_1^2\left(2\bar{I}_{45}\frac{4}{3h^2}-K_2/3-3\left(\frac{4}{3h^2}\right)^2\bar{I}_{55}-\bar{I}_{44}/3\right)}{4R_1^2}-\frac{R_1^2\pi\left(\bar{B}_{11}+\bar{B}_{22}+2\bar{B}_{12}\right)}{5R_0^2},$$

$$\bar{b}_{311}=\frac{\pi}{3}R_1^2,\ \bar{b}_{312}=\int_{-h/2}^{h/2}\rho_{sh}dz+\frac{b_p}{d_p}\int_{-h/2}^{h/2}\rho_{st}dz.$$

By solving Eqs. (21) and (22), the amplitudes U and Φ are obtained, then, substituting them into Eq. (23), leading to

$$\begin{aligned}&W\left(\bar{b}_{32}\bar{c}_{21}+\bar{b}_{38}+\bar{b}_{31}\bar{c}_{11}\right)+K_3W^3\bar{b}_{37}+\bar{b}_{311}q\\&+\left(h\kappa+W\right)W\left(\bar{b}_{33}\bar{c}_{11}+\bar{b}_{34}\bar{c}_{21}\right)\\&+\left(2\kappa h+W\right)W\left(\bar{b}_{31}\bar{c}_{12}+\bar{b}_{32}\bar{c}_{22}\right)\\&+\left(W+4\kappa h/3\right)W\bar{b}_{35}\\&+\left(\kappa h+W\right)\left(2\kappa h+W\right)W\left(\bar{b}_{36}+\bar{b}_{33}\bar{c}_{12}+\bar{b}_{34}\bar{c}_{22}\right)\\&=\left(\dot{W}c+\ddot{W}\bar{b}_{312}\right)\frac{R_1^2\pi}{5},\end{aligned}\tag{24}$$

where

$$\bar{c}_{11}=\frac{\bar{b}_{12}\bar{b}_{23}-\bar{b}_{13}\bar{b}_{22}}{\bar{b}_{11}\bar{b}_{22}-\bar{b}_{12}^2},\bar{c}_{12}=\frac{\bar{b}_{12}\bar{b}_{24}-\bar{b}_{14}\bar{b}_{22}}{\bar{b}_{11}\bar{b}_{22}-\bar{b}_{12}^2},$$

$$\bar{c}_{21}=\frac{\bar{b}_{12}\bar{b}_{13}-\bar{b}_{11}\bar{b}_{23}}{\bar{b}_{11}\bar{b}_{22}-\bar{b}_{12}^2},\ \bar{c}_{22}=\frac{\bar{b}_{12}\bar{b}_{14}-\bar{b}_{11}b_{24}}{\bar{b}_{11}\bar{b}_{22}-\bar{b}_{12}^2}.$$

For the forced vibration analysis, a time-dependent harmonic excitation $q=Q\sin\Omega t$ is introduced into Eq. (24), and the resulting governing equation is solved using the Runge-Kutta method to obtain the time-deflection responses of the structures. The harmonic external pressure considered in this study is representative of periodic excitations commonly encountered in engineering practice, such as those induced by rotating machinery, fluctuating fluid pressure, or acoustic loading.

For linear and free vibration, the viscous damping contribution, nonlinear terms, and applied excitation are neglected, leading to a linear homogeneous equation of motion. Accordingly, the natural frequency can be expressed as

$$\omega = \sqrt{-\frac{5\left(\bar{c}_{11}\bar{b}_{31} + \bar{c}_{21}\bar{b}_{32} + \bar{b}_{38}\right)}{\bar{b}_{312}\pi R_1^2}}. \tag{25}$$

Consider the perfect circular plates and spherical shell caps ($\kappa = 0$), Eq. (24) can be rewritten by

$$\begin{aligned} &H_1 W + H_2 W^2 + H_3 W^3 + H_4 Q \sin\Omega t \\ &+ H_5 \ddot{W} + H_6 c\dot{W} = 0 \end{aligned} \tag{26}$$

where

$$\begin{aligned} &H_1 = \bar{c}_{11}\bar{b}_{31} + \bar{b}_{38} + \bar{c}_{21}\bar{b}_{32}, \\ &H_2 = \bar{c}_{21}\bar{b}_{34} + \bar{c}_{11}\bar{b}_{33} + \bar{c}_{22}\bar{b}_{32} + \bar{c}_{12}\bar{b}_{31} + \bar{b}_{35} \\ &H_3 = \bar{c}_{22}\bar{b}_{34} + \bar{b}_{36} + \bar{c}_{12}\bar{b}_{33} + \bar{b}_{37}K_3, \\ &H_4 = \bar{b}_{311},\ H_5 = -\frac{\pi R_1^2 \bar{b}_{312}}{5},\ H_6 = -\frac{\pi R_1^2}{5}. \end{aligned}$$

The vibration amplitude is also assumed to be in a harmonic form

$$W = A_1 \sin(\Omega t) + A_2 \cos(\Omega t). \tag{27}$$

Substituting the vibration amplitude form (27) into Eq. (26), neglecting the higher-order terms, and applying the harmonic balance method leads to

$$\begin{aligned} &-H_5 A_1 \Omega^2 - H_6 c A_2 \Omega + H_1 A_1 + \frac{3}{4} H_3 A_1^3 \\ &+ \frac{3}{2} H_3 A_1 A_2^2 + H_4 Q = 0 \end{aligned} \tag{28}$$

$$\begin{aligned} &-H_5 A_2 \Omega^2 + H_6 c A_1 \Omega + H_1 A_2 \\ &+ \frac{3}{2} H_3 A_1^2 A_2 + \frac{3}{4} H_3 A_2^3 = 0 \end{aligned} \tag{29}$$

The polar coordinate system is applied to two amplitude components as $A_1 = A\sin(\Psi)$, $A_2 = A\cos(\Psi)$, and substituting them into Eqs. (28) and (29), then their approximated forms can be presented as

$$\begin{aligned} &A\sin(\psi)\left(H_1 - H_5\Omega^2 + \frac{15H_3A^2}{16}\right) \\ &-A\cos(\psi)H_6 c\Omega = -H_4 Q \end{aligned} \tag{30}$$

$$\begin{aligned} &A\cos(\psi)\left(H_1 - H_5\Omega^2 + \frac{15H_3A^2}{16}\right) \\ &+A\sin(\psi)H_6 c\Omega = 0 \end{aligned} \tag{31}$$

The frequency-amplitude relation is obtained from Eqs. (30) and (31), as Eq. (32)

$$\begin{aligned} \Omega = \frac{1}{2}\Bigg[&\frac{2}{H_5^2}\left(2H_1H_5 + \frac{15H_3H_5A^2}{8} - H_6^2c^2\right) \\ &\pm\sqrt{\frac{4H_6^4c^4 - 16H_1H_5H_6^2c^2}{H_5^4} - \frac{15H_3H_6^2c^2A^2}{H_5^3} + \frac{16H_4^2Q^2}{A^2H_5^2}}\Bigg]^{\frac{1}{2}}. \end{aligned} \tag{32}$$

4. Numerical results and discussions

Table 1 validates the present formulation by comparing the fundamental frequency parameters of FG-GPLRC circular plates with those reported in Refs. [23] and [24]. The comparison is conducted for different GPL distribution patterns (FG-X, UD, and FG-O) and various radius-to-thickness ratios. It is evident that the results obtained herein show excellent agreement with the existing data, with only marginal discrepancies attributable to differences in modeling assumptions and numerical implementation. This close correlation confirms the accuracy of the higher-order shear deformation framework, the adopted material modeling via the Halpin-Tsai scheme, and the solution procedure employed.

Table 2 reports the fundamental natural frequencies of FG-GPLRC shallow circular spherical shell caps for different GPL distribution patterns (U/U, X/X, O/O, V/Λ, and Λ/V), considering both unstiffened and parallel-stiffened configurations and several GPL mass fractions

W_{GPL}. For the unstiffened shells, the frequency increases monotonically as W_{GPL} rises from 0% to 0.9%, demonstrating the expected stiffness enhancement due to graphene platelet reinforcement; among the graded patterns, the X/X combination yields the highest frequencies, while O/O tends to produce the lowest values, reflecting their relative effectiveness in improving bending stiffnesses. When parallel stiffeners are introduced, a substantial upward shift in frequency is observed for all distribution patterns and GPL contents, confirming the strong stiffening contribution of the ribs in elevating the global dynamic stiffness. Notably, the ranking among distribution patterns remains broadly consistent in the stiffened case (with X/X and V/Λ generally higher than O/O), indicating that material gradation and stiffener reinforcement act in a complementary manner.

Fig. 3 provides a comprehensive illustration of the nonlinear frequency-amplitude characteristics of the FG-GPLRC circular plates and shallow spherical shell caps under harmonic excitation, clearly revealing the combined influences of structural reinforcement, geometric parameters, foundation nonlinearity, excitation level, and damping.

In Fig. 3(a), the presence of parallel stiffeners shifts the response curves toward higher frequencies and reduces the vibration amplitudes at resonance. Physically, the stiffeners increase the global bending stiffnesses and membrane stiffness, thereby enhancing the overall dynamic stiffness of the system. As a result, the effective restoring force becomes stronger, leading to a pronounced hardening-type nonlinear behavior characterized by a rightward bending of the backbone curve.

Fig. 3(b) further shows that decreasing the stiffener spacing intensifies this stiffening effect. From a mechanical standpoint, closer stiffeners provide a more uniform redistribution of bending and membrane stresses, limiting transverse deflection and increasing the effective structural resistance to dynamic loading. Consequently, the resonance frequency increases and the nonlinear response becomes less sensitive to amplitude growth.

The influence of shell geometry is evident in Fig. 3(c), where variations in the base radius modify the curvature effect. A smaller base radius corresponds to higher curvature, which introduces additional membrane action under transverse deflection. This membrane-bending coupling enhances geometric stiffness, thereby increasing the natural frequency and amplifying the hardening response. In contrast, as the shell approaches a flat plate configuration, the geometric stiffening effect diminishes.

Fig. 3(d) highlights the role of the nonlinear foundation stiffness. A positive cubic foundation stiffness (hardening foundation) augments the restoring force at large deflections, resulting in a stronger hardening-type frequency shift. Conversely, a negative cubic stiffness (softening foundation) reduces the effective restoring force at higher amplitudes, causing the resonance curve to bend leftward and potentially leading to jump phenomena and multi-valued responses. This behavior reflects the competition between structural geometric nonlinearity and foundation-induced nonlinearity.

Finally, Figs. 3(e) and 3(f) demonstrate the effects of excitation amplitude and damping. Increasing the excitation amplitude intensifies the contribution of cubic nonlinear terms, thereby enlarging the frequency shift and accentuating nonlinearity. In contrast, higher damping coefficients suppress resonance peaks, reduce amplitude magnification, and mitigate jump discontinuities by dissipating vibrational energy. Physically, damping stabilizes the dynamic response and narrows the range of unstable solutions.

Fig. 4 presents the time-domain dynamic responses of the FG-GPLRC circular plates and shallow spherical shell caps under harmonic excitation, emphasizing the influences of stiffener configuration, geometric parameters, material gradation, nonlinear foundation effects, shell curvature, and excitation frequency.

In Fig. 4(a), the introduction of parallel stiffeners noticeably reduces the steady-state vibration amplitude and accelerates the stabilization of oscillations. This behavior can be physically attributed to the increased global stiffness and load redistribution capability provided by the stiffeners, which enhance resistance to transverse deformation.

Table 1. Validation of fundamental frequency parameters $\bar{\omega}=\omega a_0^2\sqrt{h\rho_m/D_m}$ of FG-GPLRC circular plates (W^*_{GPL} =1%, ν_m =0.34, ρ_m =1200kg/m^3, E_m =3GPa, a_0 =1m, $D_m=E_m h^3/\left[12\left(1-\nu_m{}^2\right)\right]$).

Type	References	a_0/h		
		29.4118	10	5
FG-X	Javani et al. [24]	24.7333	23.9322	21.7190
	Chien and Phuc [23]	24.1789	23.1168	20.6648
	Present	25.1197	24.1887	21.6710
UD	Javani et al. [24]	21.16378	20.6418	19.1378
	Chien and Phuc [23]	21.2205	20.5657	19.0329
	Present	21.4086	20.9684	19.6549
FG-O	Javani et al. [24]	16.8334	16.5524	15.7053
	Chien and Phuc [23]	17.7029	17.3051	16.3881
	Present	16.8242	16.6377	16.0492

Table 2. Fundamental natural frequencies of FG-GPLRC stiffened and unstiffened spherical shell caps with different GPL mass fractions and GPL distribution patterns (rad/s, $R_0=R_1/0.05$, $R_1=20h$, $h=0.01$m, $\kappa=0$, $h_p=2h$, $b_p=h$, $d_p=R_1/6$, K_1 = 10 MN/m^3, K_2 = 0.1 MN/m, K_3 = 0 N/m^5)

	W_{GPL}	U/U	X/X	O/O	V/Λ	Λ/V
Unstiffened	0%	3352.94	3352.94	3352.94	3352.94	3352.94
	0.3%	3649.78	3744.45	3546.71	3635.67	3639.17
	0.6%	3922.93	4088.28	3728.95	3879.62	3886.58
	0.9%	4177.12	4396.66	3901.50	4097.54	4107.90
Parallel stiffeners	0%	4221.84	4221.84	4221.84	4221.84	4221.84
	0.3%	4605.03	4614.52	4588.50	4652.93	4537.99
	0.6%	4958.05	4968.76	4922.47	5031.87	4822.18
	0.9%	5287.01	5293.18	5230.60	5373.82	5083.55

Fig. 4(b) shows that decreasing stiffener spacing further suppresses vibration amplitudes, as a denser stiffening layout improves bending stiffnesses and limits dynamic deflection.

The effect of the base radius, illustrated in Fig. 4(c), reveals that shells with smaller radii (i.e., higher curvature) exhibit lower vibration amplitudes and higher oscillation frequencies. This phenomenon is associated with curvature-induced membrane action, which contributes additional geometric stiffness during large deflections.

In Fig. 4(d), the nonlinear foundation stiffness significantly modifies the oscillation pattern: a positive cubic stiffness strengthens the restoring force at large amplitudes, leading to more stable and bounded oscillations, whereas a negative cubic term promotes softening behavior and may increase response amplitudes.

Fig. 4(e) highlights the influence of shell radius, confirming that increased curvature enhances dynamic stability through membrane–bending coupling.

Finally, Fig. 4(f) demonstrates that when the excitation frequency approaches the natural frequency, resonance amplification occurs, resulting in large steady-state amplitudes; deviations from resonance reduce the response magnitude.

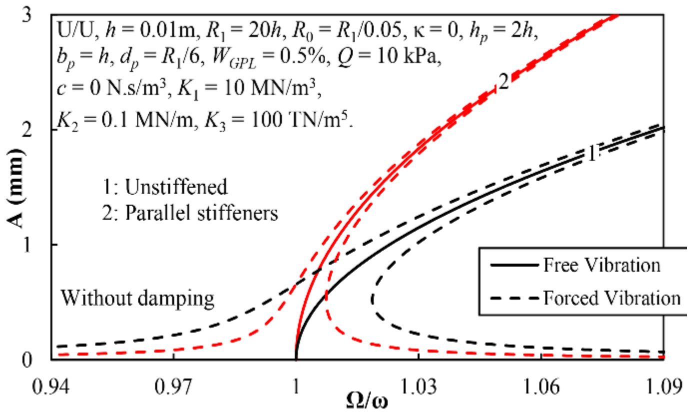

(a) Effect of stiffener

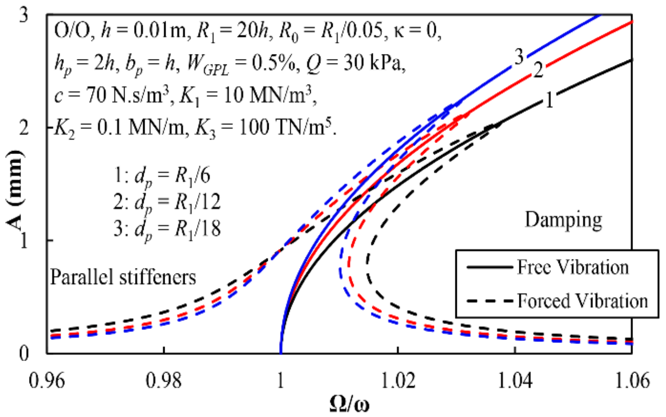

(b) Effect of stiffener spacing

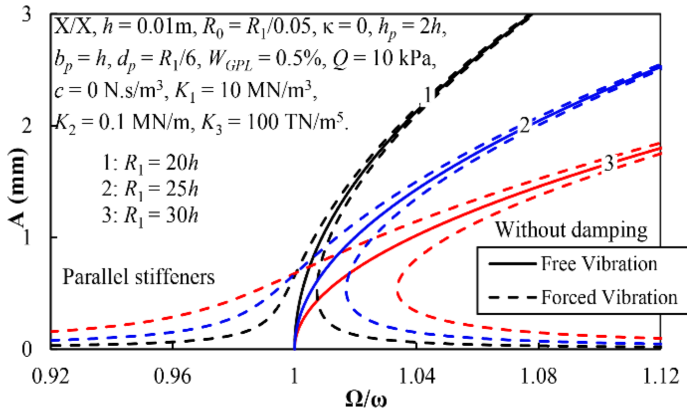

(c) Effect of base radius

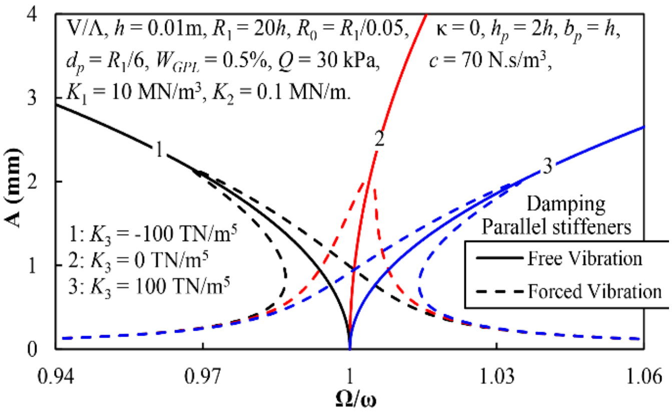

(d) Effect of nonlinear foundation stiffness

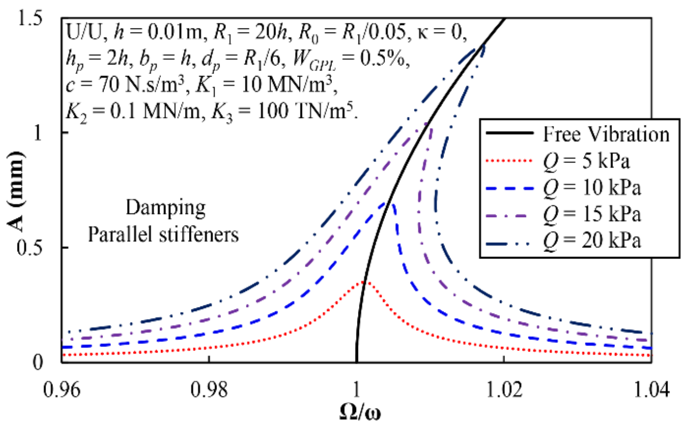

(e) Effect of amplitude of excitation force

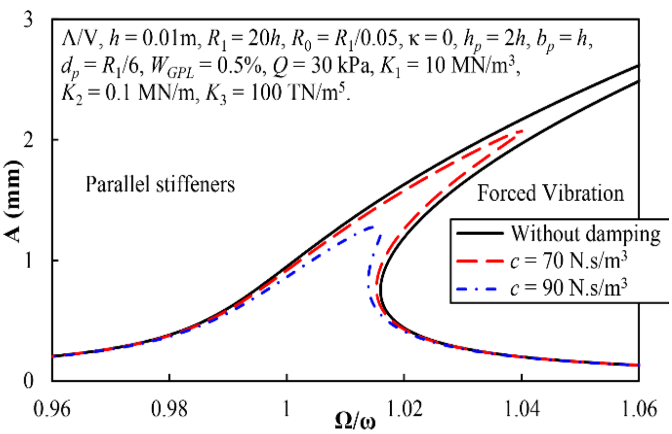

(f) Effect of damping coefficient

Fig. 3. Effects of the stiffener, base radius, and amplitude of forced load on the frequency-amplitude curves of plates and shell caps

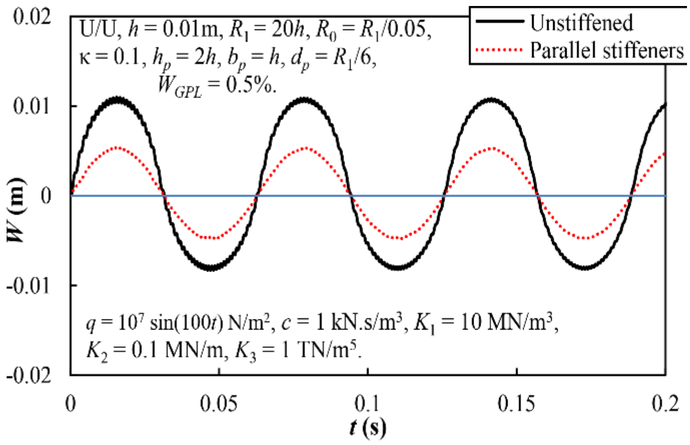

(a) Effect of stiffener

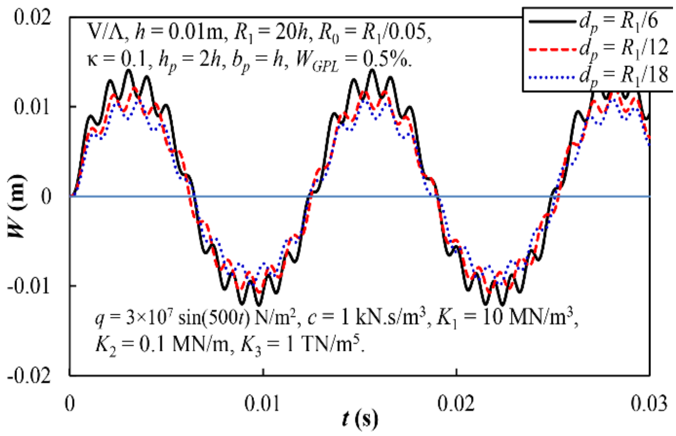

(b) Effect of stiffener spacing

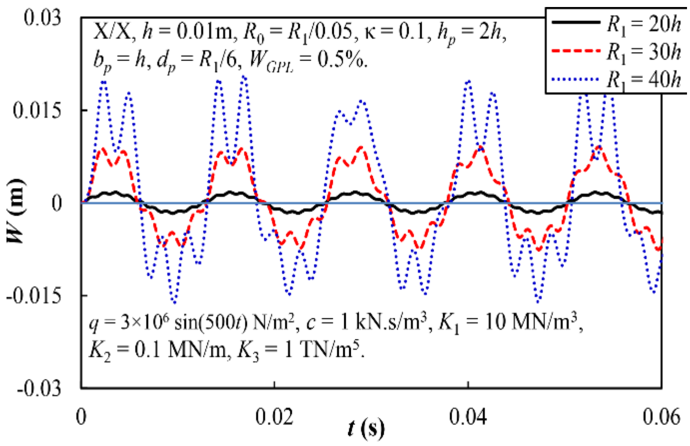

(c) Effect of base radius

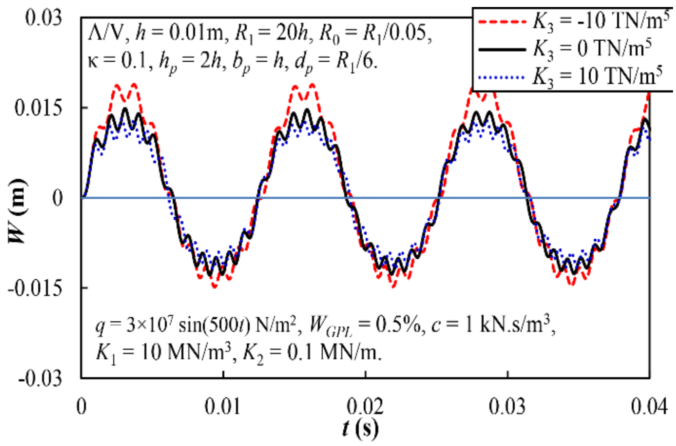

(d) Effect of nonlinear foundation stiffness

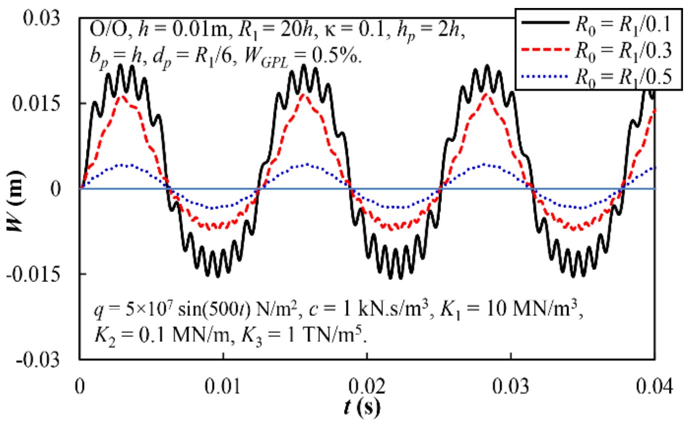

(e) Effect of shell's radius

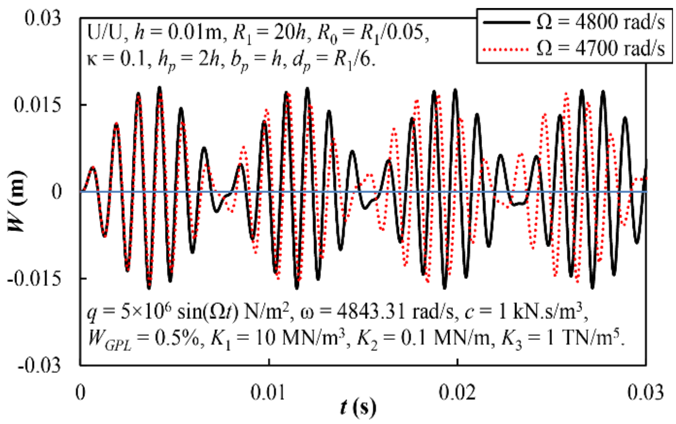

(f) Effect of excitation frequency

Fig. 4. Effects of stiffeners, geometrical and material properties on the dynamic responses of plates and shell caps under harmonic loads

5. Conclusion

In this study, a comprehensive semi-analytical formulation has been developed to investigate the nonlinear forced vibration behavior of FG-GPLRC circular plates and shallow spherical shell caps reinforced with parallel stiffeners and resting on a nonlinear viscoelastic foundation. The governing equations were established based on higher-order shear deformation theory incorporating von Kármán geometric nonlinearity, while the stiffeners were modeled using an improved smeared stiffener technique. The effects of viscous damping and nonlinear elastic foundation were consistently introduced through the Rayleigh dissipation function and Euler-Lagrange formulation. The nonlinear dynamic responses were obtained via the Runge-Kutta method, and the frequency-amplitude relationships were derived using the harmonic balance method.

The numerical results demonstrate that both graphene platelet gradation and stiffener reinforcement significantly enhance the structural stiffness, leading to increased natural frequencies and reduced vibration amplitudes. The nonlinear foundation stiffness strongly influences the dynamic characteristics, producing either hardening or softening behavior depending on its sign. Moreover, geometric curvature and excitation conditions play a critical role in shaping the resonance response and stability of the system.

Overall, the proposed model provides an efficient and simple analytical framework for predicting the nonlinear dynamic behavior of stiffened FG-GPLRC plate and shell structures, and it can serve as a useful reference for the optimal design of advanced composite structural components operating under dynamic loading conditions.

Declaration of Generative AI

During the preparation of this work, the authors did not use Generative AI and AI-assisted technologies to generate the content of the manuscript.

References

[1]. J.N. Reddy, E. Ruocco, J.A. Loya, A.M.A. Neves. (2021). Theories and analyses of functionally graded circular plates. *Composites Part C: Open Access*, 5, 100166. https://doi.org/10.1016/j.jcomc.2021.100166

[2]. M.M. Ghomshei. (2020). A numerical study on the thermal buckling of variable thickness Mindlin circular FGM plate on a two-parameter foundation. *Mechanics Research Communications*, 108, 103577. https://doi.org/10.1016/j.mechrescom.2020.103577

[3]. M. Shariyat, M.M. Alipour. (2013). Semi-analytical consistent zigzag-elasticity formulations with implicit layerwise shear correction factors for dynamic stress analysis of sandwich circular plates with FGM layers. *Composites Part B: Engineering*, 49, 43-64. https://doi.org/10.1016/j.compositesb.2013.01.001

[4]. Y. Kiani. (2017). Axisymmetric static and dynamics snap-through phenomena in a thermally postbuckled temperature-dependent FGM circular plate. *International Journal of Non-Linear Mechanics*, 89, 1-13. https://doi.org/10.1016/j.ijnonlinmec.2016.11.003

[5]. R. Lal, R. Saini. (2020). Vibration analysis of FGM circular plates under non-linear temperature variation using generalized differential quadrature rule. *Applied Acoustics*, 158, 107027. https://doi.org/10.1016/j.apacoust.2019.107027

[6]. C. Chu, M.S.H. Al-Furjan, R. Kolahchi, A. Farrokhian. (2023). A nonlinear Chebyshev-based collocation technique to frequency analysis of thermally pre/post-buckled third-order circular sandwich plates. *Communications in Nonlinear Science and Numerical Simulation*, 118, 107056. https://doi.org/10.1016/j.cnsns.2022.107056

[7]. A. Belounar, F. Boussem, M.N. Houhou, A. Tati, L. Fortas. (2022). Strain-based finite element formulation for the analysis of functionally graded plates. *Archive of Applied Mechanics*, 92, 2061-2079. https://doi.org/10.1007/s00419-022-02160-y

[8]. R. Shahsiah, M.R. Eslami, R. Naj. (2006). Thermal instability of functionally graded shallow spherical shell. *Journal of Thermal Stresses*, 29(8), 771-790. https://doi.org/10.1080/01495730600705406

[9]. M.S. Boroujerdy, M.R. Eslami. (2014). Thermal buckling of piezoelectric functionally graded material deep spherical shells. *The Journal of Strain Analysis for Engineering Design*, 49(1), 51-62.

https://doi.org/10.1177/0309324713484905

[10]. V.H. Nam, N.T. Phuong, D.H. Bich. (2020). Buckling analysis of parallel eccentrically stiffened functionally graded annular spherical segments subjected to mechanic loads. *Mechanics of Advanced Materials and Structures*, 27(7), 569-578. https://doi.org/10.1080/15376494.2018.1487608

[11]. N.T. Phuong, V.H. Nam, D.T. Dong. (2020). Nonlinear vibration of functionally graded sandwich shallow spherical caps resting on elastic foundations by using first-order shear deformation theory in thermal environment. *Journal of Sandwich Structures & Materials*, 22(4), 1157-1183. https://doi.org/10.1177/1099636218782645

[12]. T.Q. Minh, D.T. Dong, V.M. Duc, N.V. Tien, N.T. Phuong, V.H. Nam. (2022). Nonlinear Axisymmetric Vibration of Sandwich FGM Shallow Spherical Caps with Lightweight Porous Core. *CIGOS 2021, Emerging Technologies and Applications for Green Infrastructure, Lecture Notes in Civil Engineering*, 203, 381-389. https://doi.org/10.1007/978-981-16-7160-9_38

[13]. L.N. Ly, D.T.N. Thu, D.T. Dong, V.M. Duc, B.T. Tu, N.T. Phuong, V.H. Nam. (2023). A Novel Analytical Approach for Nonlinear Thermo-Mechanical Buckling of Higher-Order Shear Deformable Porous Circular Plates and Spherical Caps with FGM Face Sheets. *International Journal of Applied Mechanics*, 15(05), 2350035. https://doi.org/10.1142/S1758825123500357

[14]. R. Gholami, R. Ansari. (2017). Large deflection geometrically nonlinear analysis of functionally graded multilayer graphene platelet-reinforced polymer composite rectangular plates. *Composite Structures*, 180, 760-771. https://doi.org/10.1016/j.compstruct.2017.08.053

[15]. R. Ansari, R. Hassani, R. Gholami, H. Rouhi. (2021). Buckling and Postbuckling of Plates Made of FG-GPL-Reinforced Porous Nanocomposite with Various Shapes and Boundary Conditions. *International Journal of Structural Stability and Dynamics*, 21(05), 2150063. https://doi.org/10.1142/S0219455421500632

[16]. J. Liu, Y. Zhang, Y. Zhang, S. Kitipornchai, J. Yang. (2023). Aeroelastic analyses of functionally graded aluminium composite plates reinforced with graphene nanoplatelets under fluid-structural interaction. *Aerospace Science and Technology*, 136, 108254. https://doi.org/10.1016/j.ast.2023.108254

[17]. Y. Liu, Y. Chen, C. Shao, A.M. Alshamrani. (2024). The efficient data-driven solution to estimate the nonlinear bending of sandwich doubly curved panel subjected to transient loading. *Aerospace Science and Technology*, 147, 108980. https://doi.org/10.1016/j.ast.2024.108980

[18]. M. Javani, Y. Kiani, M. R. Eslami. (2020). Thermal buckling of FG graphene platelet reinforced composite annular sector plates. *Thin-Walled Structures*, 148, 106589. https://doi.org/10.1016/j.tws.2019.106589

[19]. Y. Wang, R. Zeng, M. Safarpour. (2022). Vibration analysis of FG-GPLRC annular plate in a thermal environment. *Mechanics Based Design of Structures and Machines*, 50(1), 352-370. https://doi.org/10.1080/15397734.2020.1719508

[20]. M. Saadatfar, M.H. Zarandi. (2020). Deformations and Stresses of an Exponentially Graded Magneto-Electro-Elastic Non-Uniform Thickness Annular Plate Which Rotates with Variable Angular Speed. *International Journal of Applied Mechanics*, 12(05), 2050050. https://doi.org/10.1142/S1758825120500507

[21]. Y.W. Zhang, G.L. She, M.A. Eltaher. (2023). Nonlinear transient response of graphene platelets reinforced metal foams annular plate considering rotating motion and initial

geometric imperfection. *Aerospace Science and Technology*, 142(Part B), 108693. https://doi.org/10.1016/j.ast.2023.108693

[22]. J.P. Song, G.L. She, M.A. Eltaher. (2024). Nonlinear aero-thermo-elastic flutter analysis of stiffened graphene platelets reinforced metal foams plates with initial geometric imperfection. *Aerospace Science and Technology*, 147, 109050. https://doi.org/10.1016/j.ast.2024.109050

[23]. T.H. Chien, P.V. Phuc. (2020). A meshfree approach using naturally stabilized nodal integration for multilayer FG GPLRC complicated plate structures. *Engineering Analysis with Boundary Elements*, 117, 346-358. https://doi.org/10.1016/j.enganabound.2020.04.001

[24]. M. Javani, Y. Kiani, M.R. Eslami. (2021). Geometrically nonlinear free vibration of FG-GPLRC circular plate on the nonlinear elastic foundation. *Composite Structures*, 261, 113515. https://doi.org/10.1016/j.compstruct.2020.113515

[25]. L.N. Ly, B.T. Tu, D.T.N. Thu, D.T. Dong, V.M. Duc, N.T. Phuong. (2023). Nonlinear thermo-mechanical buckling and postbuckling of sandwich FG-GPLRC spherical caps and circular plates with porous core by using higher-order shear deformation theory. *Journal of Thermoplastic Composite Materials*, 36(10), 4083-4105. https://doi.org/10.1177/08927057221147827

[26]. N.T. Phuong, D.T. Dong, B.T. Tu, V.M. Duc, L.N. Khuong, P.T. Hieu, V.H. Nam. (2024). Nonlinear thermo-mechanical axisymmetric stability of FG-GPLRC spherical shells and circular plates resting on nonlinear elastic medium. *Ships and Offshore Structures*, 19(6), 820-830. https://doi.org/10.1080/17445302.2023.2214489

[27]. D. Liu, Y. Zhou, J. Zhu. (2021). On the free vibration and bending analysis of functionally graded nanocomposite spherical shells reinforced with graphene nanoplatelets: Three-dimensional elasticity solutions. *Engineering Structures*, 226, 111376. https://doi.org/10.1016/j.engstruct.2020.111376

[28]. V.H. Nam, T.Q. Minh, P.T. Hieu, V.T. Hung, B.T. Tu, N.T.T. Hoai, D.T. Dong. (2023). A new analytical approach for nonlinear thermo-mechanical postbuckling of FG-GPLRC circular plates and shallow spherical caps stiffened by spiderweb stiffeners. *Thin-Walled Structures*, 193, 111296. https://doi.org/10.1016/j.tws.2023.111296

[29]. N.T.T. Hoai, D.T. Dong, C.V. Doan, N.V. Tien, V.H. Nam (2026). A new semi-analytical approach for nonlinear vibration behavior of porous graphene platelet reinforced circular plates and spherical caps with stepped spiderweb stiffeners. *Journal of Vibration and Control, 2026*. https://doi.org/10.1177/10775463251405339

[30]. K.Q. Thai, B.T. Tu, C.C. Anh. (2026). Nonlinear thermo-mechanical buckling responses of FG-GPLRC catenary caps and circular plates. *Journal of Science and Transport Technology,* 6(2), 98-115. https://doi.org/10.58845/jstt.utt.2026.en.6.2.98-115